Cerebral Cortex, September 2021;31: 4259–4273

https://doi.org/10.1093/cercor/bhab084
Advance Access Publication Date: 14 May 2021
Original Article

ORIGINAL ARTICLE

A Distinct Population of L6 Neurons in Mouse V1 Mediate Cross-Callosal Communication

Yajie Liang[1,5], Jiang Lan Fan[3], Wenzhi Sun[1,4,6], Rongwen Lu[1,7], Ming Chen[4] and Na Ji[1,2]

[1]Janelia Research Campus, Howard Hughes Medical Institute, Ashburn, VA 20147, USA, [2]Department of Physics, Department of Molecular and Cell Biology, Helen Wills Neuroscience Institute, University of California, Berkeley, CA 94720, USA, [3]UCSF-UC Berkeley Joint PhD Program in Bioengineering, University of California, Berkeley, CA 94720, USA, [4]iHuman Institute, ShanghaiTech University, Shanghai 201210, China, [5]Current address: Department of Diagnostic Radiology and Nuclear Medicine, University of Maryland, Baltimore, MD 201210, USA, [6]Current address: Chinese Institute for Brain Research, Beijing 102206, China and [7]Current address: National Eye Institute, National Institutes of Health, Bethesda, MD 20892, USA

Address correspondence to Na Ji, Department of Physics, Department of Molecular Cell Biology, Helen Wills Neuroscience Institute, University of California, Berkeley. Email: jina@berkeley.edu.

Abstract

Through the corpus callosum, interhemispheric communication is mediated by callosal projection (CP) neurons. Using retrograde labeling, we identified a population of layer 6 (L6) excitatory neurons as the main conveyer of transcallosal information in the monocular zone of the mouse primary visual cortex (V1). Distinct from L6 corticothalamic (CT) population, V1 L6 CP neurons contribute to an extensive reciprocal network across multiple sensory cortices over two hemispheres. Receiving both local and long-range cortical inputs, they encode orientation, direction, and receptive field information, while are also highly spontaneous active. The spontaneous activity of L6 CP neurons exhibits complex relationships with brain states and stimulus presentation, distinct from the spontaneous activity patterns of the CT population. The anatomical and functional properties of these L6 CP neurons enable them to broadcast visual and nonvisual information across two hemispheres, and thus may play a role in regulating and coordinating brain-wide activity events.

Key words: callosal projection neurons, corpus callosum, corticothalamic neurons, layer 6, visual cortex

Introduction

As the largest bundle of axonal fibers in the mammalian brain, the corpus callosum mediates interhemispheric communications through axonal projections between cortices of the frontal, parietal, occipital, and temporal lobes (Zaidel and Iacoboni 2003). Early anatomical studies suggested that callosal projection (CP) neurons are primarily L2/3 or L5 neurons projecting homotopically to the contralateral cortex (Yorke Jr and Caviness Jr 1975; Ramos et al. 2008; Fame et al. 2011). Later functional studies indicated that these neurons participate in collaborative processing of information across the hemispheres. For sensory cortices, the transcallosal pathways are thought to enable the processing of bilateral sensory stimuli. For example, CP neurons in the somatosensory cortex were found to mediate bilateral integration of tactile information (Shuler et al. 2001; Hlushchuk and Hari 2006). In the auditory cortex, CP neurons were shown to contribute to sound localization in spatial hearing (Rock and Apicella 2015).

In visual cortices, callosal connections highly concentrate at the borders between the primary and secondary visual cortices (Yorke Jr and Caviness Jr 1975; Lewis and Olavarria 1995; Wang and Burkhalter 2007). Because this border region contains a

representation of the vertical midline of visual field, these CP neurons, mainly located in L2/3 and L5, were considered to be involved in binocularity and fusion of visual fields (Lewis and Olavarria 1995; Stryker and Antonini 2001; Pietrasanta et al. 2012; Dehmel and Lowel 2014). Inactivation experiments indicated that these callosal inputs strongly modulate visual cortical responses (Payne et al. 1991; Zhao et al. 2013; Dehmel and Lowel 2014). However, whether and how the monocular V1 contributes to callosal projection remains partially known. In rodents, the monocular part of V1 was initially considered as acallosal (Yorke Jr and Caviness Jr 1975). CP neurons were later found throughout the deep infragranular layer in V1 (Cusick and Lund 1981; Olavarria and Van Sluyters 1983). Compared to other cortical cell types, very little is known about the identity, connectivity, or activity of these CP cells (Harris and Shepherd 2015).

In this study, we used a high-efficiency recombinant AAV variant to gain genetic access to CP neurons in the mouse monocular V1, studied their connectivity profiles with a combination of viral strategies, and characterized their activity in awake mice using in vivo calcium imaging. We found that V1 CP neurons were concentrated in L6 and formed a distinct population from the *NTSR1*-positive corticothalamic (CT) L6 neurons. We used rabies viral tracing to identify their presynaptic partners and found cells in both local V1 circuit and long-range cortical areas. Although a substantial proportion of L6 CP neurons encoded visual features such as orientation tuning and possessed well-defined receptive fields, an even larger fraction exhibited spontaneous activity that was often modulated by the presence of visual stimuli. Consistent with the functional results, L6 CP neurons were discovered to contribute to an extensive transcallosal network across two hemispheres, projecting to and receiving inputs from multiple cortical regions of different sensory modalities.

Materials and Methods

All experimental protocols were conducted according to the National Institutes of Health guidelines for animal research and approved by the Institutional Animal Care and Use Committee at Janelia Research Campus, Howard Hughes Medical Institute, as well as by the Animal Care and Use Committee at the University of California, Berkeley.

Experimental Model and Subject Details

The following mouse lines were used: Wild-type C57BL/6 J (Jackson Laboratory); NTSR1-Cre (strain B6.FVB(Cg)-Tg(NTSR1-cre)GN220Gsat/Mmcd, stock number 030648-UCD); Scnn1a-Tg3-Cre mice (Jax no. 009613); Rbp4-Cre mice (MMRRC no. 031125-UCD); Gad2-IRES-Cre (Jax no. 010802); tdTomato reporter line (Ai14, Jax. 007908); nuclear tdTomato reporter line (R26 LSL H2B mCherry 1H3 line, Jax no. 023139); Ai3 mice (JAX Stock No: 007903). Mice of both sexes (older than P60) were used. Sample sizes (number of mice, cells and/or field-of-view, FOVs) for each experiment are stated in main text. AAV viruses were obtained from Virus Services of Janelia Research Campus, HHMI.

Virus Injection for Histology

Virus injection and cranial window implantation procedures have been described previously (Sun et al. 2016). Briefly, mice were anesthetized with isoflurane (1–2% by volume in O_2) and given the analgesic buprenorphine (SC, 0.3 mg per kg of body weight). Virus injection was performed using a glass pipette (Drummond Scientific Company) beveled at 30° with a 15- to 20-μm opening and back-filled with mineral oil. A fitted plunger controlled by a hydraulic manipulator (Narishige, MO10) was inserted into the pipette and used to load and inject the viral solution.

For the injection of virus for histological examination, a burr hole was made (~200 μm diameter) over the injection site. 30 nl virus-containing solution (rAAV2-retro.CAG.GFP, 1×10^{13} infectious units per ml) was injected 0.6 mm below pia at two injection sites for each brain region. The injection coordinates for each brain region are: 1). V1: midline: 2.5 mm, Bregma: −3.4 mm and −4.0 mm; 2). V2M: midline: 1.25 mm, Bregma: −3.4 mm and −4.0 mm; 3). V2L: midline 3.5 mm, Bregma: −3.4 mm and −4.0 mm; 4). Auditory cortex: midline 4.0 mm, Bregma: −3.4 mm and −4.0 mm.

For rabies tracing experiment, 1:1 mixture of AAV2/1.CAG.FLEX.BFP.T2A.TVA (5×10^{13} infectious units per ml) and AAV2/1.CAG.FLEX.BFP.T2A.G (7.2×10^{12} infectious units per ml) were injected into left V1 at the coordinates described above (30 nl at 0.6 mm below pia). For the labeling of CP neurons, rAAV2-retro.syn.Cre (1×10^{13} infectious units per ml) was first injected into right V1 at the same coordinates, before rabies vectors were injected. Three weeks later, ΔRV.mCherry (3.4×10^{8} infectious units per ml) was injected into the same injection sites in left V1 (30 nl, 0.6 mm below pia).

Viral Injection and Cranial Window Implantation for In Vivo Imaging

For the labeling of CT and CP cells for calcium imaging, a 3.5-mm diameter craniotomy was first made over left V1 of NTSR1-Cre and wildtype mice, respectively. Then 30 nl of virus-containing solution (AAV2/1.syn.FLEX.GCaMP6s, 1×10^{13} infectious units per ml) was injected 0.6 mm below pia into left V1 at four injection sites at the intersection points of the two left–right lines at Bregma −3.4 mm and −4.0 mm, and two anterior–posterior lines at 2.2 mm and 2.6 mm from the midline. For the labeling of CP neurons, rAAV2-retro.syn.Cre (1×10^{13} infectious units per ml) was first injected into the contralateral V1 at the same coordinates, before craniotomy was performed. For dual-color imaging experiments, a 1:1 mixture of AAV2/1.CAG.FLEX.jRGECO1a and AAV2/1.CAG.FRT.GCaMP6s was injected into left V1 of NTSR1-Cre mice, and rAAV2-retro.syn.FLPo was injected into the right V1 of the same animal. After the pipette was pulled out of the brain, a glass window made of a single coverslip (Fisher Scientific, no. 1.5) was embedded in the craniotomy and sealed in place with dental acrylic. A titanium headpost was then attached to the skull with cyanoacrylate glue and dental acrylic.

Visual Stimulation

Visual stimuli were presented either by a tablet computer (Samsung Galaxy Book2) with an AMOLED screen displaying only blue light or by back projection on a screen made of Teflon film using a custom-modified DLP projector. The screen was positioned 17 cm from the right eye, covering 75° × 75° of visual space and oriented at ~40° to the long body axis of the animal. The projector provided equilength and linear frames at 360 Hz (designed by A. Leonardo, Janelia Research Campus, and Lightspeed Design, model WXGA-360). Its lamp housing was replaced by a holder for liquid light guide, through which visible

light (450–495 nm) generated by a LED light source (SugarCUBE) was delivered to a screen made of polytetrafluoroethylene. The maximal luminance measured at the location of animal eyes was 437 nW/mm^2. Visual stimuli were generated using custom-written codes. During visual stimulation, the luminance level was kept constant. To measure orientation-tuning, full-field square drifting gratings were presented in 12 directions in a pseudorandom sequence for 6 s each. Gratings had 100% contrast, 0.07 cycles per degree, and drifted at 26 degrees per second (i.e., a temporal frequency of ~2 Hz). Each oriented drifting grating was presented for a total of 10 trials. Between the drifting grating stimuli, static gratings or a gray screen was presented for 6 s.

Pupil Tracking

An infrared-sensitive CCD camera controlled by either a custom MATLAB script or a custom written interface with LabVIEW collected images of the pupil illuminated by an infrared LED array or two-photon excitation light scattered into the eye during brain imaging at 10-Hz frame rate. The pupil was segmented by custom-written MATLAB codes and pupil diameter values interpolated to find the diameter of the pupil corresponding to each two-photon image.

Two-Photon Imaging

All imaging experiments were carried out on head-fixed, awake mice, except receptive field mapping data, for which mice were anesthetized. To habituate the mice to experimental handling, each mouse was head-fixed onto the sample stage with its body restrained under a half-cylindrical cover, which reduced struggling and prevented substantial body movements such as running. The habituation procedure was started 1 week after surgery, repeated 3–4 times for each animal, and each time for 15–60 min. Imaging was performed with a two-photon fluorescence microscope 3–4 weeks after virus injection. Each experimental session lasted 45 min to 2 h. Multiple sections (imaging planes) may be imaged within the same mouse. GCaMP6s was excited at 940 nm with a femtosecond laser system (InSight Deepsee, Spectra-Physics) or at 920 nm with a femtosecond laser (Chameleon Ultra II, Coherent) that was focused by either a Nikon 16×, 0.8 NA or an Olympus 25×, 1.05 NA objective. Emitted fluorescence photons reflected off a dichroic long-pass beamsplitter (FF665-Di02–25 × 36; Semrock) and were detected by a photomultiplier tube (H7422PA-40, Hamamatsu). jRGECO was excited at 1100 nm with the same laser source. For simultaneous imaging of GCaMP6s and jRGECO, 1030 nm was used for excitation.

Images of CP or CT neurons were acquired from 550 to 650 µm below pia. Laser power measured post objective varied between 67 mW and 329 mW (n = 38 imaging sessions from 17 mice). Typical time for mapping the orientation selectivity of a single image section was ~25 min, during which no photobleaching or photodamage was observed. 256 × 256 pixels at 1.2–2.2 µm per pixel and 2–3 Hz frame rate were used for some imaging sessions, while 512 × 512 pixels at 0.47–0.94 µm per pixel and 29 Hz frame rate were used for others.

Histology

The survival time before histological evaluation for mice injected with tracers (e.g., fluorogold) and AAVs was 1 week and 3 weeks, respectively. For mapping of presynaptic neurons, Cre-dependent AAVs encoding rabies glycoprotein (G) and the avian virus receptor (TVA) were injected into mice with target cells expressing Cre. Three weeks later, modified rabies virus (ΔRV) encoding mCherry was injected into the same mouse, resulting in the targeted infection of the previously labeled neurons, and subsequent trans-synaptic spread and expression of mCherry. The brain was fixed after 8 days post rabies virus injection. For histological examination, mice were deeply anesthetized with isoflurane and transcardially perfused with PBS and then 4% paraformaldehyde (w/v). Brains were removed and post-fixed overnight in 4% paraformaldehyde. Fixed whole brains were embedded in 4% agar and sliced with vibrating microtome (V1200S, Leica) at the thickness of 100 µm for direct observation or 40 µm for immunostaining. We performed immunostaining by application of primary antibodies (overnight): chicken-anti-GFP (Aves, 1:200) for GCaMP6s, or anti-GABA (Abcam, 1:200) to identify interneurons. After three washes for 5 min each in phosphate-buffered saline (PBS), secondary antibodies were applied along with 0.1% Triton X-100 for 1 h. For secondary antibodies, we used Alexa Fluro 488-conjugated donkey anti-chicken (Invitrogen, 1:500) or Alexa Fluro 594-conjugated donkey anti-rabbit (Invitrogen, 1:500). All brain slices were mounted in Vector Shield mounting solution. Coronal images were acquired via a stereomicroscope at low zoom (×2–4), at high zoom with Zeiss ApoTome.2 (20×/0.8NA, optical section step of 0.5 µm), or on a confocal microscope (Zeiss LSM 800, 63×/1.4 NA oil immersion, optical section step of 0.5 µm). For brain sections from rabies-tracing experiments, we manually counted the presynaptic cells. To determine their cortical regions and layer locations, we first identified the coronal plane of each brain section using the mouse brain atlas (Franklin and Paxinos 2012), with which we then determined the cortical region of each neuron. Finally, to determine the cortical layer of each neuron, we used the Allen mouse brain atlas (http://atlas.brain-map.org/). We counted 282 ± 56, 409 ± 76, and 242 ± 42 mCherry$^+$ cells (mean ± s.e.m.) when CT, CP, and L4 pyramidal cells were starter cells, respectively.

Analysis of Two-Photon Imaging Data

Imaging data were processed with custom programs written in MATLAB (Mathworks) and Fiji (Schindelin et al. 2012). Images were registered with an iterative cross-correlation-based registration algorithm (Sun et al. 2016). Cortical neurons were outlined by hand as regions of interest (ROIs). The averaged fluorescence signal within the ROI was calculated as the raw ROI signal F_{raw}. Neuropil subtraction was performed as follows. First, a square region centered on an ROI and roughly twice the area of the ROI was determined. Then, the average fluorescence signal of the region, not including the ROI, was calculated as the raw neuropil signal $F_{neuropil}$. The neuropil signal was then baseline-subtracted by subtracting the average of the lowest 5% values of the neuropil signal time trace to get $\Delta F_{neuropil}$. Neuropil-subtracted fluorescence signal within the ROI was then calculated as $F = F_{raw} - 0.7 * \Delta F_{neuropil}$. For each ROI, we used the mode from the fluorescence intensity histogram of F as the baseline fluorescence F_0, and calculate its calcium transient as $\Delta F/F$ (%) = $(F - F_0)/F_0 \times 100$ as previously described (Sun et al. 2016). For highly spontaneously active ROIs, the mode of the fluorescence intensity histogram did not represent the basal fluorescence. For these neurons, we used the average of the lowest 10 percentile intensity values as F_0.

For each ROI, we calculated "Mean99prc," the mean of the $\Delta F/F$ values that were 99% or above in the distribution of its $\Delta F/F$ values during an imaging session. A neuron was considered active if its Mean99prc was above 50% (see Supplementary Fig. 1, e.g., active and nonactive neurons). We compared this criterion with our previously used one (the maximum of mean $\Delta F/F$ during the presentation of visual stimuli was above 10% (Sun et al. 2016)) on data of CT neurons under drifting grating stimulation (1503 cells, 10 mice). We found very similar percentages of active neurons (85.3% vs. 83.6%, current versus prior criterion), suggesting that the two criteria were equivalent in identifying active neurons. As the new criterion allowed the evaluation of spontaneous activity (i.e., activity of neurons while the animal was in the dark), we used this criterion throughout our analysis.

A neuron was considered as visually-evoked by drifting grating if its activity during at least one drifting grating stimulus was significantly higher than their activity during the interstimulus period by paired t test ($P < 0.01$) (Tan et al. 2015) (see Supplementary Fig. 2, e.g., neurons with visually-evoked and spontaneous activity).

Analysis of Orientation Selectivity of Individual Neurons

The orientation selectivity index (OSI), directional selectivity index (DSI), global OSI, global DSI, and tuning full width at half maxima (FWHM) was defined based on previous publications (Niell and Stryker 2008; Marshel et al. 2011; Sun et al. 2016). Briefly, the response R of each ROI to a visual stimulus was defined as the average $\Delta F/F$ across the 6-s window of drifting grating presentation. The final response to each visual stimulus used for tuning analysis was the average of 10 trials. For ROIs with significantly different responses across the drifting directions (one-way ANOVA, $P < 0.05$), we fit their normalized response tuning curves to grating drifting angle θ with a bimodal Gaussian function. Only neurons whose tuning curve was well fit by this function were defined as orientation selective. The tuning width for the preferred orientation is calculated as the FWHM of the Gaussian function. OSI was computed as $(R_{pref} - R_{ortho})/(R_{pref} + R_{ortho})$, with R_{pref} and R_{ortho} being the responses at the preferred and orthogonal orientations, respectively. With this index, perfect orientation selectivity would give OSI = 1; an equal response to all orientations would have OSI = 0. DSI was defined as $(R_{pref} - R_{oppo})/(R_{pref} + R_{oppo})$, where R_{pref} and R_{oppo} are the responses at the preferred motion direction and its opposite, respectively. Global OSI was calculated as the magnitude of the vector average divided by the sum of all responses: $gOSI = |\Sigma_k R(\theta_k) e^{i2\theta k}|/\Sigma_k R(\theta_k)$, where $R(\theta_k)$ is the measured response at orientation θ_k, and global DSI was defined as $|\Sigma_k R(\theta_k) e^{i\theta k}|/\Sigma_k R(\theta_k)$.

Receptive Field Mapping

For receptive field mapping, sparse-noise stimulation sequences were presented during two-photon calcium imaging (Tan et al. 2015). Each visual stimulus lasted for 400 ms and consisted of a pair of dark and bright square pixels randomly distributed within a gray 10×10 grid, extending $\sim 75°$ of visual field. The total stimulation time was around 30 min. Imaging frames were acquired at approximately 7 Hz for receptive mapping. Neuronal responses were inferred from calcium signals using the fast non-negative deconvolution method (Vogelstein et al. 2010). Jackknife analysis was then used to resample the neuronal responses 10 times and each time omitting a different 10% of the response (David et al. 2004; Bonin et al. 2011). For each resampled response set, spike-triggered averages for ON and OFF stimuli were calculated separately (Reid and Shapley 1992) at various time delays from −2 to 5 frames prior to neuronal responses. The ON and OFF receptive subfields obtained at the time delays that yielded the highest peak response amplitudes were chosen. The final receptive subfields were the averages of these 10 pairs of receptive subfields. Only subfields that pass thresholding at six z-scores were considered to have well-defined receptive fields.

Statistical Tests

Standard functions and custom-written scripts in MATLAB were used to perform all analysis. The data were tested for normal distribution. Parametric tests were used for normally distributed data and non-parametric tests were applied to all other data. Bar graphs and mean ± standard error of the mean (SEM) were used to describe the data with normal distribution, while box plots and median ± interquartile range (IQR) were used to describe the non-normally distributed data. Box plots represent median and 25th—75th percentiles and their whiskers shown in Tukey style (plus or minus 1.5 times IQR). A nonparametric test (Wilcoxon signed-rank test) was used to examine paired data. Direct non-paired comparisons between two groups were made using Wilcoxon rank-sum test for non-normally distributed data. The statistical significance was defined as $^*P < 0.05$, $^{**}P < 0.01$, $^{***}P < 0.001$, respectively. Experiments were not performed blind. Sample sizes were not predetermined by statistical methods, but were based on those commonly used in the field. Medians, IQR, means and SEM are reported throughout the text.

Results

CP Neurons in Mouse V1 Are Dominantly Located in L6

Traditionally, CP neurons were labeled with intra-parenchymal injection of retrograde tracers, such as horseradish peroxidase or Fluoro-Gold (FG), with varying efficacy (Kobbert et al. 2000). To label CP neurons with high efficacy, we took advantage of a recently developed recombinant AAV variant (rAAV2-retro) that permits efficient retrograde access to projection neurons (Tervo et al. 2016). We injected rAAV2-retro carrying GFP (rAAV2-retro.CAG.GFP) into the monocular zone of right V1 of a transgenic mouse line with L5 excitatory neurons labeled with H2B-mCherry (Rbp4-Cre × Rosa26 LSL CAG H2B mCherry (Peron et al. 2015). We observed brightly labeled CP neurons in the left monocular V1 predominantly located in the cortical layer below L5, with few cells in the supragranular layer (L2/3) (Fig. 1A). More superficial CP neurons were observed at the border of V1 and V2L, consistent with earlier studies (Yorke Jr and Caviness Jr 1975; Lewis and Olavarria 1995; Wang and Burkhalter 2007). Immunostaining with anti-GABA antibody indicated that these neurons were not GABAergic (Supplementary Fig. 3A,B). Therefore, CP neurons in mouse V1 are dominantly excitatory neurons located in L6.

L6 CP Neurons and NTSR1-Positive CT Neurons are Distinct Populations

Having identified L6 neurons as the main callosal-projecting neurons in mouse monocular V1, we then asked whether these

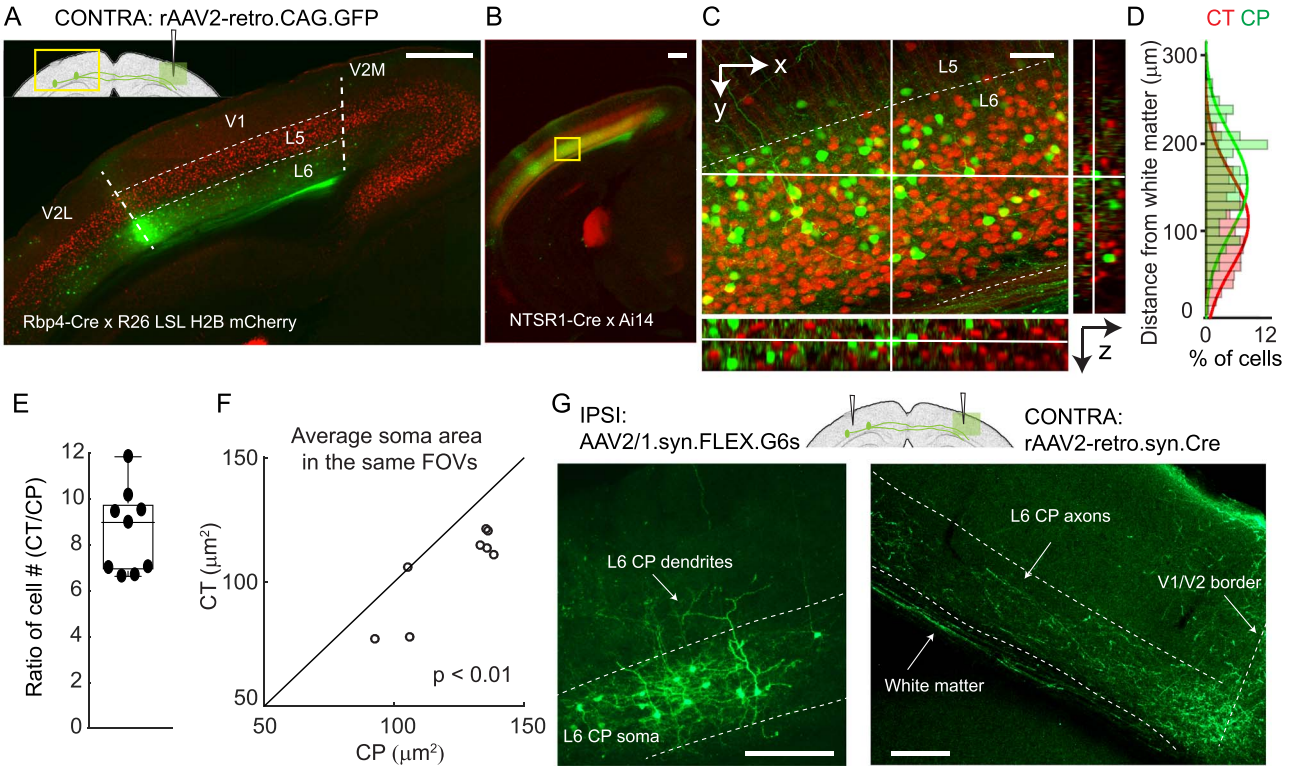

Figure 1. A distinct population of CP neurons in L6 of the mouse monocular V1. (*A*,*B*) Fluorescence images of left V1 after rAAV2-retro.CAG.GFP injection in contralateral (CONTRA) V1 with L5 pyramidal neurons labeled with H2B-mCherry (*A*; Rbp4-Cre × R26 LSL H2B mCherry) and L6 CT neurons labeled with tdTomato (*B*; NTSR1-Cre × Ai14), respectively. (*C*) Magnified and orthogonal views of the yellow box area in (*B*) (CP in green, CT in red). (*D*) Depth distributions of 515 CT and 80 CP somata measured by cell counting from the volume in (*C*). (*E*) Ratio of cell counts (CT vs. CP) from the nine FOVs, $n = 4$ mice (1–2 FOVs from each mouse, 4718 CT and 611 CP neurons). (*F*) Average cell size comparison between CP and CT neurons in the same FOVs. 4440 CT and 802 CP neurons in the nine FOVs from four mice. Wilcoxon signed-rank test, $P = 0.0078$. (*G*) Contralateral injection of rAAV2-retro.syn.Cre and ipsilateral injection of AAV2/1.syn.FLEX.GCaMP6s labeled CP neurons (left panel) in ipsilateral (IPSI) V1 and their axons in contralateral V1 (right panel). Axon image is taken after immunostaining with anti-GFP antibody. Dashed lines: (*A*,*G*) V1/V2 borders and cortical layers. Scale bar: 500 μm in (*A*,*B*); 50 μm in (*C*); 200 μm in (*G*).

CP neurons were distinct from the thalamus-projecting L6 CT neurons. To this end, we utilized a Cre-recombinase transgenic mouse line NTSR1-Cre (NTSR1-cre GN220) that selectively labels L6 CT neurons in V1 (Gong et al. 2007; Olsen et al. 2012; Bortone et al. 2014). Crossed with the Cre reporter line Ai14 (Madisen et al. 2010), the resulting mice had L6 CT neurons expressing red fluorescent protein tdTomato. Injecting rAAV2-retro.syn.GFP in the right V1 and labeling CP neurons in the left hemisphere, we similarly observed that CP neurons were mostly located in L6 (Fig. 1*B*), with high-resolution image stacks showing a clear separation of CP and CT neurons in V1 (Fig. 1*C*). Across 10 FOVs from four mice including a total of 4718 CT and 611 CP neurons, we did not observe a single cell double-labeled with GFP and tdTomato. Similar separation was also observed with FG as the retrograde tracer (Supplementary Fig. 3*C*,*D*). These results indicate that L6 CP neurons are distinct from *NTSR1*-positive CT neurons.

Counting the number of cells along the cortical depth, we found slightly different distributions for these two groups of neurons: more CP neurons were found in superficial L6, while there were more CT neurons at depth (Fig. 1*D*). In the same fields-of-view (FOVs), CT neurons were ~nine times denser than CP (median = 9.0, interquartile range IQR = 3.0, 4 mice, 9 FOVs, Fig. 1*E*). On average, CP neurons had significantly larger somata (Wilcoxon signed-rank test, $P < 0.01$, 10 FOVs from the four mice, Fig. 1*F*), consistent with the data from CP neurons in the rat somatosensory cortex (Zhang and Deschenes 1997). Contralateral injection of rAAV2-retro.syn.Cre and ipsilateral injection of AAV2/1.syn.FLEX.GCaMP6s labeled CP neurons with green fluorescent protein GCaMP6s. The dendrites of some CP neurons extended into L5 (Fig. 1*G*, left panel) and their projections to the contralateral cortex are mainly localized in the infragranular layers (Fig. 1*G*, right panel).

L6 CP Neurons Receive Both Local and Long-Range Cortical Inputs

We next investigated the upstream inputs of L6 CP neurons using rabies viral tracing (Wickersham et al. 2007). We used rAAV2-retro.syn.cre to express Cre recombinase in L6 CP neurons in wildtype mouse V1. We also utilized the Scnn1a-Cre transgenic mouse line that expressed Cre recombinase in L4 pyramidal neurons and the NTSR1-Cre transgenic mouse line that expressed Cre recombinase in L6 CT neurons. Injections of Cre-dependent AAV helper vectors drove expression of glycoprotein (G), avian receptor protein (TVA), and blue fluorescent protein (BFP) in the starter cell population expressing Cre. Three weeks later, we injected a glycoprotein deficient form of the rabies virus encapsulated with the avian sarcoma and leucosis virus envelope protein (ΔRV), which expressed mCherry in neurons presynaptic to the starter cells as well as the starter cells themselves. Consequently, the starter cells were identified

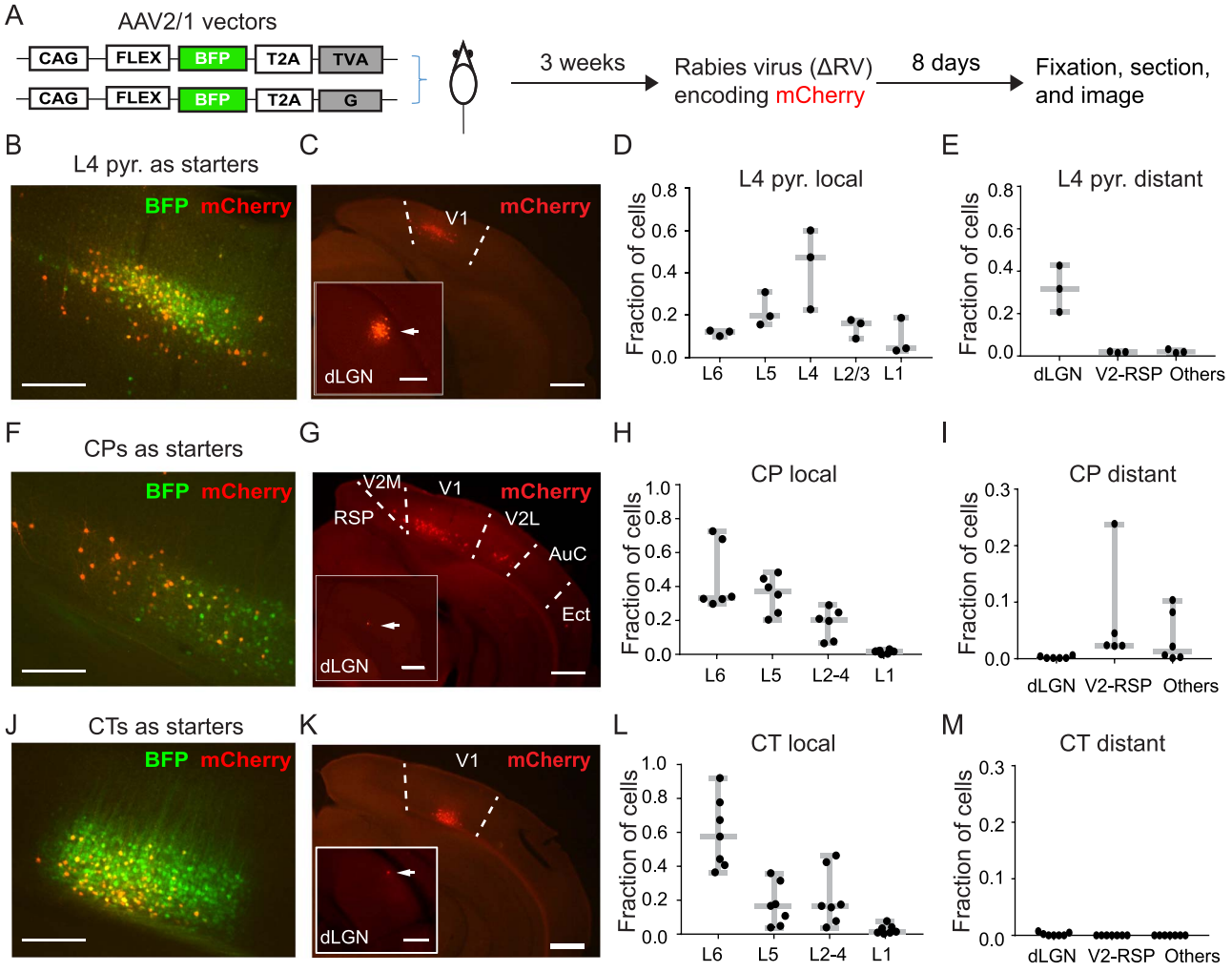

Figure 2. Presynaptic partners of V1 L6 CP neurons from the ipsilateral hemisphere. (*A*) Schematic showing the experimental procedure. Starter cells were double-labeled by BFP and mCherry. mCherry$^+$-only labeling indicated presynaptic partners of starter neurons. (*B,C*) Example fluorescence images of coronal brain sections with L4 pyramidal neurons as starter cells (*B*) and their presynaptic neurons ipsilateral to the injection site (*C*). (*D,E*) Fractions of local (*D*; within V1) and long-range (*E*) presynaptic neurons of L4 pyramidal neurons. (*F,G*) Example fluorescence images of coronal brain sections with CP neurons as starter cells (*F*) and their presynaptic neurons ipsilateral to the injection site (*G*). (*H,I*) Fractions of local (*H*) and long-range (*I*) presynaptic neurons of L6 CP neurons. (*J,K*) Example fluorescence images of coronal brain sections with CT neurons as starter cells (*J*) and their presynaptic neurons ipsilateral to the injection site (*K*). (*L,M*) Fractions of local (*L*) and long-range (*M*) presynaptic neurons of L6 CT neurons. Arrows in insets of (*C,G,K*) point to presynaptic cells in dLGN. Scale bars: 200 μm in (*B,F,J*) and insets of (*C,G,K*); 500 μm in (*C,G,K*).

as those expressing both BFP and mCherry, and the presynaptic cells were those labeled only with mCherry. The mice were perfused 8 days later and the brains sectioned and imaged to chart the spatial locations of the presynaptic neurons (Fig. 2A).

To validate our rabies tracing method, we investigated the presynaptic cell population for L4 pyramidal neurons. With L4 pyramidal cells as the starter cells (Fig. 2B), we observed prominent local (493 out of 726 mCherry$^+$ cells, $n = 3$ mice, Fig. 2C,D) and long-range presynaptic cells (especially in dLGN, 214 out of 726 mCherry$^+$ cells, $n = 3$ mice, Fig. 2C inset and Fig. 2E). This agreed with the known connectivity of these neurons (Lien and Scanziani 2013) and confirmed the validity of our rabies tracing method.

With CP cells in V1 as starter cells (Fig. 2F), we found strong local V1 inputs (2150 out of 2459 mCherry$^+$ cells, $n = 6$ mice, Fig. 2G,H), as well as substantial ipsilateral long-range inputs from V2 (V2M, V2L) and retrosplenial cortex (RSP) (262 out of 2459 mCherry$^+$ cells, $n = 6$ mice) as well as auditory cortex (AuC) and ectorhinal cortex (Ect) (47 out of 2459 mCherry$^+$ cells, $n = 6$ mice; Fig. 2G,I). We also found a few presynaptic neurons in the contralateral hemisphere located in the infragranular layer (Supplementary Fig. 4). These results indicate that CP neurons receive both local V1 and long-range cortical inputs.

In contrast, using CT neurons in V1 as starter cells (Fig. 2J), we found that nearly all of the labeled presynaptic cells (1971 out of 1974 mCherry$^+$ cells, $n = 7$ mice) were located locally spanning all layers of V1 (Fig. 2K,L). We found a few long-range projecting presynaptic cells in thalamus (three out of 1974 mCherry$^+$ cells, inset in Fig. 2K showing one example neuron in dLGN), but none in secondary visual or retrosplenial cortices (Fig. 2M). These results indicate that CP neurons receive more long-range inputs than CT neurons.

Together with the rAAV2-retro experiments, these results suggested that distinct from CT neurons, CP neurons receive

both local and long-range cortical inputs, while simultaneously transferring information to and integrating information from CP neurons in the contralateral hemisphere.

Drifting-Grating-Evoked Responses of L6 CP and CT Neurons in V1 of Awake Mice

Having characterized the L6 CP neurons anatomically, we then investigated their visually evoked responses and compared them with L6 CT neurons, using in vivo calcium imaging (Fig. 3). L6 CT neurons in V1 of the left hemisphere were transfected with the calcium indicator GCaMP6s (Chen et al. 2013) by injecting AAV2/1.syn.FLEX.G6s in V1 of the NTSR1-Cre mouse (Fig. 3B). L6 CP neurons were labeled using the same approach as described above (AAV2/1.syn.FLEX.GCaMP6s in left V1 and rAAV2-retro.syn.Cre in the contralateral V1, Fig. 3D). Presenting drifting gratings to the right eye (100% contrast, 6 s drifting gratings interleaved with 6 s stationary gratings or a blank gray screen, 0.07 cycles per degree, 2 Hz, 12 directions with 10 trials each in a pseudorandom sequence), we then measured changes in fluorescence brightness ($\Delta F/F$) in the cell bodies of the GCaMP6s$^+$ neurons in quietly awake mice after habituating them to head fixation. Imaging CP and CT neurons at depths ranging from 550 to 650 μm below dura with a homebuilt two-photon fluorescence microscope optimized for deep imaging (Ji et al. 2010) (Fig. 3C,E), we identified neurons with detectable calcium transients and calculated their $\Delta F/F$ values. For each cell, if the mean of the $\Delta F/F$ values that were 99% or above in the $\Delta F/F$ distribution was above 50%, it was considered active (Materials and Methods; see, e.g., Supplementary Fig. 1). An active neuron was considered to exhibit visually-evoked activity if its activity during at least one drifting grating stimulus was significantly higher than their activity during the interstimulus interval (stationary gratings or gray screen) by paired t test ($P < 0.01$) (Materials and Methods; see Supplementary Fig. 2, e.g., neurons and population data) (Tan et al. 2015). Neurons with no significant activity difference during gray screen and drifting grating stimulus was considered to be spontaneously active. Under this criterion and with gray screen presented in between drifting grating stimuli, we found 78% of active CT neurons (358/460, 2 mice) and 26% of active CP neurons (225/878, 5 mice) to exhibit visually evoked activity.

Consistent with an earlier electrophysiological study (Velez–Fort et al. 2014), we found both CT (Fig. 3F) and CP (Fig. 3G) neurons that were selective for grating orientation and drifting direction. We explored the relationship between the tuning maps of the two groups of neurons. We labeled CP and CT neurons with GCaMP6s and jRGECO1a (Dana et al. 2016), respectively, using Cre- and FLPo-recombinase strategies (Supplementary Fig. 5A,B), and performed calcium imaging on them simultaneously. OS tests did not reveal obvious relationship between the tuning maps of CPs and CTs (Supplementary Fig. 5C–E).

For neurons with significantly different responses across different drifting gratings (one-way analysis of variance [ANOVA], $P < 0.05$), we fit their normalized response tuning curves to grating drifting angle θ with a bimodal Gaussian function and only neurons whose tuning curve were well fit by this function were defined as orientation selective. For neurons with visually evoked activity, 73% of CT (out of 358 neurons, two mice) and 39% of CP (out of 225 neurons, five mice) were orientation-selective.

We quantified orientation selectivity of each cell with orientation-selectivity index (OSI) and global OSI index (gOSI) (Materials and Methods, Fig. 3F,G). Both OSI and gOSI distributions of OS CT neurons had significantly greater medians than those of CP neurons (CT gOSI: 0.74, OSI: 0.97, 772 neurons from 10 mice; CP gOSI: 0.54, OSI: 0.84, 343 neurons from 17 mice; Wilcoxon rank-sum tests, $P < 0.001$ in both cases; static gratings presented in between drifting grating stimuli). As indicated by the OSI distributions and consistent with the distributions of the full width at half maximum (FWHM) of the tuning curves (Fig. 3J), both CT and CP populations contained highly orientation-selective and sharply tuned neurons, with their preferred orientations distributed over the entire orientation range (Fig. 3K). However, we found more broadly tuned CP neurons (FWHM around 100°, e.g., ROI i in Fig. 3G), which were absent from CT population.

Some OS neurons exhibited substantially different responses towards gratings drifting along opposite directions. Defining neurons with direction selectivity index DSI > 0.5 (or a response ratio towards opposing directions larger than 3) as direction-selective (DS), we found about half of the OS CT neurons to be DS, whereas only a quarter of the OS CP neurons were DS. Consistent with this result, DSI and gDSI distributions of OS CP cells had smaller medians than the CT cells (DSI CP: 0.25, CT: 0.49; gDSI CP: 0.17, CT: 0.40; 343 CP neurons from 17 mice, 772 CT neurons from 10 mice; Wilcoxon rank-sum tests, $P < 0.001$ in both cases; Fig. 3L,M). The FWHMs of DS neurons had similar distributions to those of the OS neurons (Fig. 3N), and their preferred motion directions were distributed throughout the whole range of angles (Fig. 3O).

Using sparse-noise stimuli consisting of a pair of white and black squares randomly distributed on a gray background, we also mapped the visual receptive fields of CT and CP neurons in anesthetized mice, using our previously published method (Tan et al. 2015). Cells with defined receptive fields were found in both groups (Supplementary Fig. 6). For CT neurons, out of 62 active cells ($n = 3$ mice), we found well-defined RFs for 26 cells (i.e., 49%); For CP neurons, out of 194 active cells ($n = 5$ mice), 13 cells were found to have well-defined RFs (i.e., 7%).

The existence of L6 CP neurons with drifting-grating-evoked activity, selectivity towards visual features, and well-defined receptive fields, as revealed by the calcium imaging experiments, suggested that some L6 CP neurons in the monocular V1 encode and transmit orientation, direction, as well as receptive field information across the corpus callosum to contralateral cortex. A distinct population from the thalamus-projecting CT neurons, CP neurons nevertheless possess similar orientation tuning characteristics and thus serve as a pathway of visual information flow between V1s of the two hemispheres.

CP Neurons Exhibit Diverse Patterns of Activity Both in the Dark and During Drifting Grating Stimuli

While investigating the orientation selectivity of L6 neurons with drifting gratings, we discovered that 74% of all active CP neurons (653/878 CP cells in five mice) had calcium transients that were not driven by drifting grating stimuli (i.e., statistically similar activity during gray screen and drifting grating stimulation, Supplementary Fig. 2) and were defined to be spontaneously active. In comparison, a much smaller fraction of active CT neurons (22%, 102/460 CT cells in two mice) exhibited spontaneous activity (Fig. 4A).

Keeping the animal in the dark, we found that, of the 883 CP neurons that were active during the combined dark and visual stimulation period, 93% of them (819 cells, five mice)

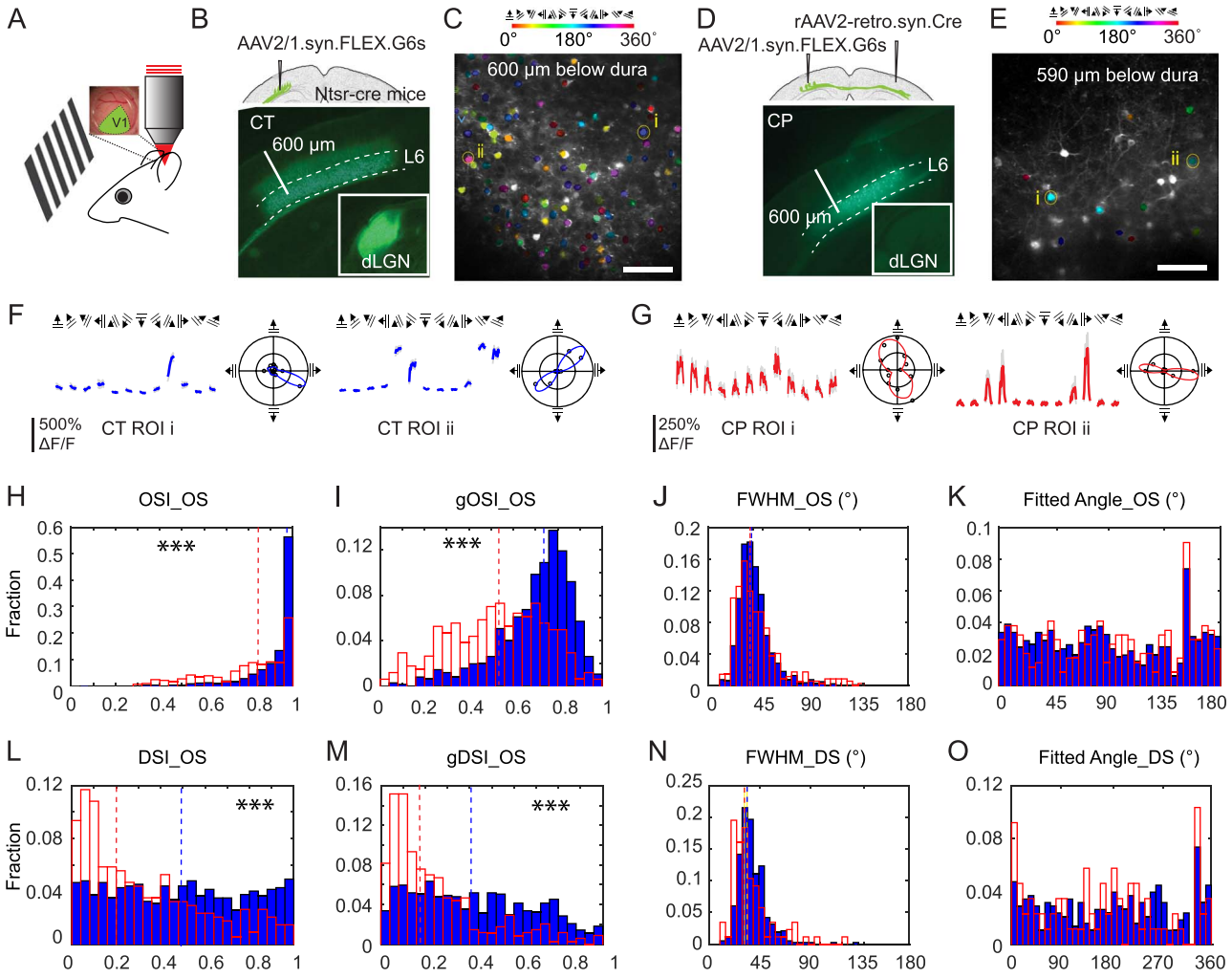

Figure 3. In vivo calcium imaging of L6 CT and CP neurons in V1 of the awake mouse. (*A*) Schematic of in vivo imaging and visual stimulation setup. (*B*,*D*) Viral labeling strategies and widefield fluorescence images of coronal sections containing GCaMP6s^{+} L6 CT (*B*) and CP (*D*) neurons. Insets: dLGN. (*C*,*E*) Example in vivo two-photon excitation fluorescence images of L6 CT (*C*) and CP (*E*) neurons, with orientation-selective (OS) neurons color-coded by their preferred grating stimuli. (*F*,*G*) (Left) Example drifting-grating-evoked calcium responses from two OS CT (*F*) and CP (*G*) neurons (i and ii, labeled in *C* and *E*). Colored lines and gray shades: average and s.d. from 10 trials. (Right) Polar plots of calcium responses and fitted turning curves. (*H*–*O*) Histogram distributions of orientation and direction tuning parameters for CT (blue) and CP (red) neurons, including OSI (*H*), gOSI (*I*), turning curve FWHMs of OS neurons (*J*), preferred orientations of OS neurons (*K*), DSI (*L*) and gDSI (*M*) of OS neurons, FWHM of DS neurons (*N*), and preferred directions for DS neurons (*O*). Dashed lines: medians. Wilcoxon rank-sum test: $^{***}P < 0.001$. Scale bars: 600 μm in (*B*,*D*); 100 μm in (*C*,*E*).

were spontaneously active in the dark. In contrast, only 41% of the CT neurons had spontaneous activity in the dark (59%, 289/489 neurons from two mice) (Fig. 4B). Furthermore, in the dark, the spontaneous calcium transients of CP neurons have higher mean ΔF/F values than CT neurons (mean ΔF/F% during the entire imaging session, median values: CP 7.6, 819 neurons from five mice; CT 3.5, 289 neurons from two mice, $P < 0.001$, Wilcoxon rank-sum test; Fig. 4C).

Next, we identified CP and CT neurons that were spontaneously active both in the dark and during grating stimulation (605 CP neurons, 94 CT neurons, Fig. 4D–F; See example traces in Supplementary Fig. 7). Similar to above (Fig. 4C), the mean ΔF/F values of these CP neurons in the dark and during grating stimulus presentation was larger than the CT population (mean ΔF/F%, median values in the dark: CP 8.4 vs. CT 5.9, $P < 0.05$; median values during grating: CP: 11.2 vs. CT: 5.2, $P < 0.001$, Wilcoxon rank-sum test; Fig. 4E). Interestingly, even though these neurons did not exhibit drifting-grating-evoked activity, the activity of a substantial fraction of CP and CT neurons were strongly modulated by the presence of grating stimuli (Fig. 4F). The spontaneous activity of 16% of CP neurons as well as 16% of CT neurons increased their mean ΔF/F increased by ≥2-fold; The spontaneous activity of 27% of CP neurons and 15% of CT neurons decreased their mean ΔF/F by ≥2-fold. The observed activity modulations by the stimulation condition suggest that they may reflect changes in the internal states that resulted from changes of the animal's sensory environment.

We found prominent differences in the spontaneous activity of CP and CT neurons that showed visually-evoked activity (Fig. 4G). Whereas these CT neurons had little spontaneous activity in the dark, both OS and NOS CP neurons had much stronger spontaneous calcium transients in the dark (mean ΔF/F%, OS neurons: CP 10.6, 87 cells from five mice, CT 2.2, 262 cells from two mice, $P < 0.001$; NOS neurons: CP 7.0, 138 cells

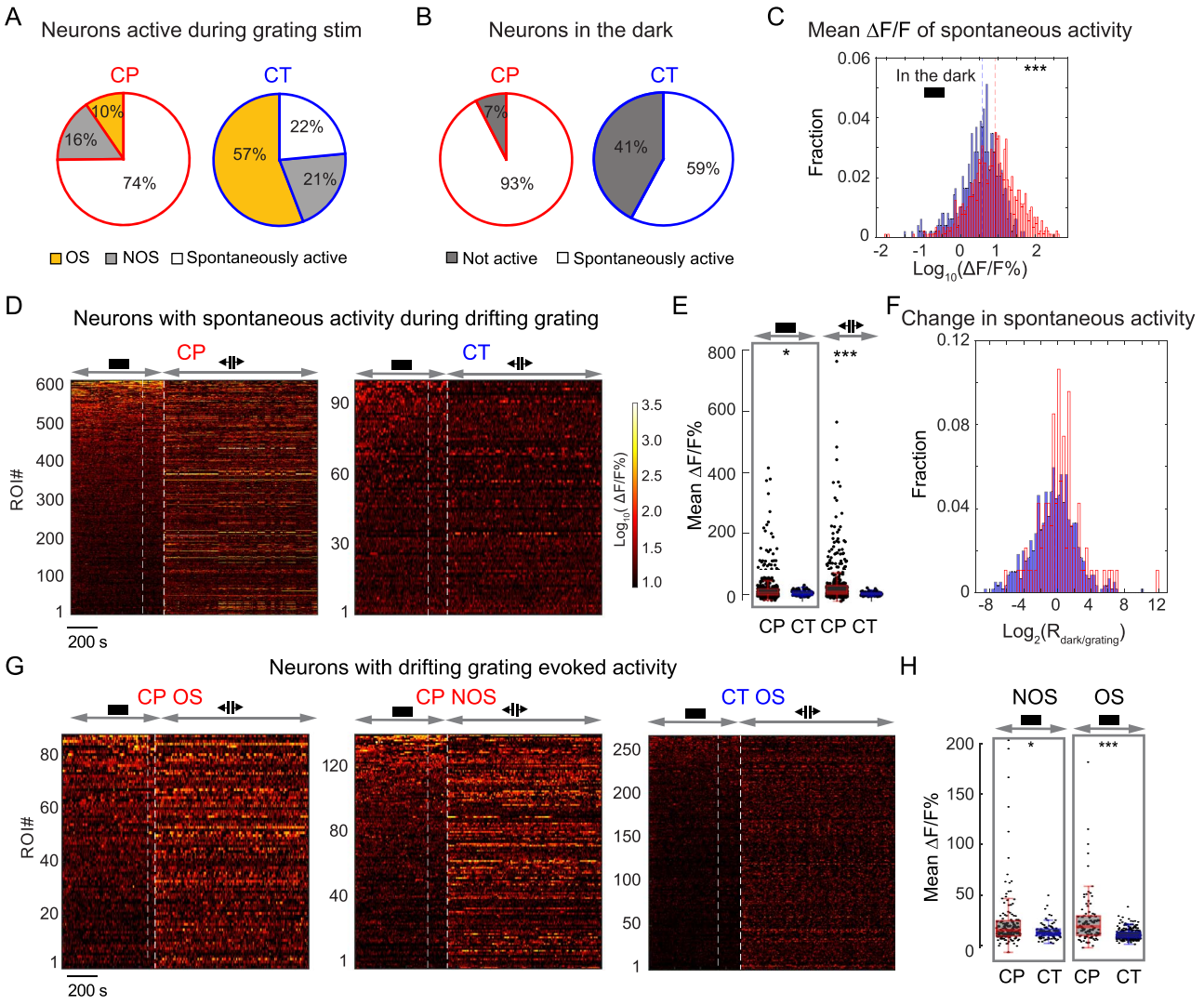

Figure 4. V1 L6 CP neurons exhibit pervasive spontaneous activity. (*A*) Percentages of active CP and CT neurons with spontaneous activity, drifting-grating-evoked OS, and drifting-grating-evoked NOS responses, respectively, during grating stimulation. (*B*) Percentages of spontaneously active neurons in the dark. (*C*) Histogram distributions of mean ΔF/F% of spontaneously active CP (red) and CT (blue) neurons in the dark. (*D*) Raster plots of calcium transients (ΔF/F%) for CP and CT neurons with spontaneous activity both in the dark and during subsequent drifting grating stimulation. (*E*) Scatter plots of mean ΔF/F% for neurons in (*D*). (*F*) Histogram distributions of the ratios of mean ΔF/F% in the dark and under grating stimuli ($R_{dark/grating}$) for CP (red) and CT (blue) neurons in (*D*). (*G*,*H*) Raster plots of calcium transients (ΔF/F%) (*G*) and scatter plots of mean ΔF/F% for CP (red) and CT (blue) neurons with visually-evoked activity (*H*). Wilcoxon rank-sum test: $^{*}P < 0.05$ and $^{***}P < 0.001$.

from five mice; CT 4.2, 96 cells from two mice, $P < 0.05$; Wilcoxon rank-sum test, Fig. 4*H*), indicating pervasive spontaneous activity as a distinct feature of L6 CP neurons. Together with the CP neurons that encoded visual information, through the cross-callosal network observed in our anatomical experiments, CP neurons thus convey both visual and non-visual information to multiple cortical regions across two hemispheres.

Activity Correlation of CP and CT Neurons with Arousal Level

Having discovered that L6 neurons exhibit strong spontaneous activity, we further investigated how their activity was correlated with the arousal level of the animal. Given that pupil diameter is a well-established measure of arousal level, with enlarged pupil correlating with heightened alertness (McGinley et al. 2015), we combined simultaneous pupillometry recording with two-photon in vivo imaging of L6 neurons in the awake mouse, with the mouse first kept in the dark and then presented with grating stimuli. Pupil was imaged with external near-infrared light illumination and pupil images segmented to calculate pupil diameter during in vivo calcium imaging (Fig. 5*A*,*B*, calcium transients and pupil diameter time courses for CT and CP neurons in example imaging FOVs).

We studied how neural activity for the individual neuron was correlated with pupil diameter by calculating the Pearson correlation coefficient between its calcium transient and the simultaneously measured pupil diameter time course. For visually evoked activity observed during grating stimulus, both CP and CT neurons have similar correlation coefficient distributions, with most neurons showing little correlation, either negative or positive, between their activity and pupil diameter

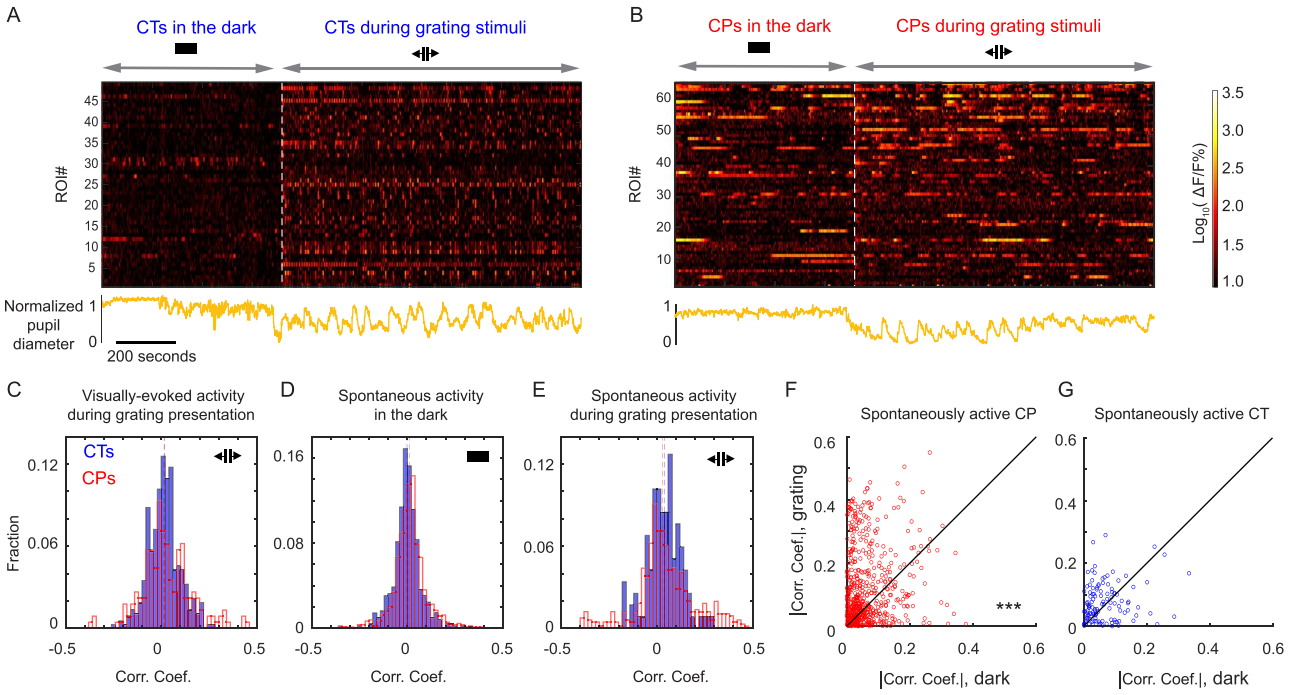

Figure 5. Activity of L6 CT and CP neurons shows distinct patterns of correlation with arousal level. (*A*,*B*) (Upper) Raster plots of calcium activity (ΔF/F%) of CT (*A*) or CP (*B*) neurons from two example FOVs recorded in the dark and during drifting grating visual stimulation. (Lower) Normalized pupil diameter (orange) recorded during the imaging sessions. (*C*) Histogram distributions of correlation coefficients between pupil diameter and drifting-grating-evoked activity for CT and CP neurons. (*D*) Histogram distributions of correlation coefficients between pupil diameter and spontaneous activity in the dark for CT and CP neurons. (*E*) Histogram distributions of correlation coefficients between pupil diameter and spontaneous activity during drifting grating stimulation. Dashed lines indicated medians for each population. (*F*,*G*) Scatter plots showing the absolute values of correlation coefficients measured in the dark against those measured during drifting grating stimulation for the same CP (*F*) and CT (*G*) neurons. Wilcoxon signed-rank test: $^{***}P < 0.0001$ for (*F*) and $P = 0.082$ for (*G*).

(neurons with correlation coefficient magnitude larger than 0.2: 7.5% for CP and 2.4% for CT; 226 CP neurons, five mice; 374 CT, two mice; Fig. 5C). Similar trends were observed for spontaneous activity for CP and CT neurons in the dark (neurons with correlation coefficient magnitude larger than 0.2: 2.6% for CP and 1.4% for CT; 886 CP neurons, five mice; 492 CT, two mice; Fig. 5D). For spontaneous activity measured during the drifting grating stimuli, however, a larger fraction of CP neurons had correlation coefficients larger than 0.2 or smaller than −0.2 (neurons with correlation coefficient magnitude larger than 0.2: 14.1% for CP and 3.4% for CT; 660 CP neurons, five mice; 118 CT cells, two mice; Fig. 5E). Comparing the spontaneous activity of the same neurons in the dark with their spontaneous activity during grating stimuli, we found that spontaneous activity of CP neurons during the presence of grating stimuli was significantly more likely to have stronger correlation with arousal (either positively or negatively, as quantified as the absolute values of their correlation coefficients, 660 CP cells, Fig. 5F) than in the dark. In contrast, the spontaneous activity of CT neurons in the dark and during visual stimulation did not exhibit statistically significant difference in their correlation with pupil diameter (118 CT cells, Fig. 5G).

Together, our investigations on the spontaneous activity characteristics of L6 neurons indicated that CP neurons possessed pervasive spontaneous activity in the dark as well as during grating stimulation, with activity patterns and correlation with arousal distinct from those of CT neurons. Together with the anatomical results presented earlier, they point to new and yet-to-explored functions of these cross-callosal neurons.

L6 CP Neurons Contribute to a Horizontal Network Interconnecting Multiple Cortical Areas across the two Hemispheres

Our rabies tracing data and functional imaging results imply substantial communications of CP neurons with neurons outside V1. We therefore carried out additional anatomical experiments to investigate the broader network of cortical CP neurons. We first asked whether there were other sources of transcallosal inputs into V1. We unilaterally injected rAAV2-retro.CAG.GFP into V1 of NTSR1-Cre × Ai14 mice (Fig. 6A), where L6 CT neurons expressed tdTomato, and found that in addition to contralateral V1, neurons in secondary visual cortical areas (V2M and V2L), auditory cortex (AuC), and ectorhinal cortex (Ect) in the contralateral hemisphere also projected to V1 (Fig. 6B). As in contralateral V1 (Fig. 6C), the CP neurons in the other cortical areas were also distinct from CT neurons (Fig. 6D–G). Interestingly, the CP populations in the contralateral primary and secondary visual cortices were all located in L6 (Fig. 6C–E), whereas the CP neurons from AuC and Ect appeared to concentrate in L5 (Fig. 6F,G). These results indicate that CP neurons from multiple cortical regions project to contralateral V1. To find out if these projections are reciprocal, we injected rAAV2-retro.CAG.GFP in V2M, V2L, or AuC cortices (Fig. 6H–J), and found GFP-labeled L6 CP neurons in V1 in the contralateral hemisphere. This indicates that V1 CP neurons broadcast information to multiple cortical regions in the contralateral brain. Together, these results indicate that V1 not only receive widespread transcallosal projections from contralateral cortical regions, but also send projections to these areas via L6 CP neurons (Fig. 6K). Therefore, L6 CP

neurons may contribute to a horizontal network interconnecting cortical regions representing multiple sensory modalities across the two hemispheres and play a role in interhemispheric cross-modal sensory integration, although more experiment are needed to support this hypothesis.

Discussion

Despite a growing recognition of the prominent roles that the corpus callosum plays in the processing of sensory information, the identity and property of CP neurons are not well understood. Traditionally considered to be L2/3 or L5 neurons projecting homotopically to the contralateral cortex, CP neurons were thought to contribute to the processing of sensory information encoding bilateral stimuli. In this work, using a designer variant of recombinant adeno-associated virus, rAAV2-retro, we gained selective genetic access to CP neurons projecting to mouse V1 and investigated their connectivity pattern and functional properties.

We found that in contrast to L2/3 and L5 CP neurons at V1/V2 border (corresponding to the binocular visual field) that contribute to binocularity, within monocular V1, the main CP neurons mediating cross-callosal communication were a population of L6 neurons that were distinct from the more well-known thalamus-projecting L6 CT neurons. Immunostaining with GABA confirmed the excitatory nature of the CP neurons, consistent with previous studies in cat and rat (Elberger 1989). Although we found the ratio of CP to CT neurons to be one to nine, the proportion of CP neurons was almost certainly underestimated due to incomplete retrograde labeling. In the context of L6 neurons in general, the CP L6 neurons identified here belong to the corticocortical (CC) population that provide only corticocortical but not corticothalamic projections. In the rat primary somatosensory cortex, an equal proportion of CT and CC neurons were found, implicating L6 as a substantial contributor of corticocortical projections (Zhang and Deschenes 1997). Our results further indicate that the CP subpopulation of the L6 CC neurons subserve cross-callosal communications for monocular V1.

When we investigated the sources of presynaptic inputs into V1 L6 neurons using rabies viral tracing, we found that, in addition to local V1 inputs, CP neurons also received long-range cortical inputs from V2 and retrosplenial cortex. In comparison, V1 CT neurons in our experiment received much less long-range input (only one long-range cell in dLGN was observed). This differs from previous work using rabies viral tracing to study the input patterns of L6 CT neurons, where more long-range inputs were found (Velez-Fort et al. 2014; Brown et al. 2020). This discrepancy may be caused by differences in the sensitivity and efficiency of rabies virus batches, especially for long-range inputs. Given that our results are consistent with the known presynaptic input patterns (e.g., monosynaptic inputs from dLGN to L4 excitatory neurons) and the same batch of virus was used for both CP and CT rabies viral tracing, it is reasonable to conclude that CP neurons receive more long-range inputs than CT neurons. However, given the small numbers of labeled cells and the unknown false negative rate of rabies viral tracing, our result does not exclude the presence of long-range inputs from other brain regions.

The retrogradely transported rAAV2-retro also allowed us to express genetically encoded calcium indicators in V1 CP neurons and study their visually evoked as well as spontaneous activity in the awake mice in vivo. Consistent with an earlier electrophysiological study on CT and cortico-cortical (CC) neurons (Velez-Fort et al. 2014), we found a substantial fraction of CT neurons to be highly selective for grating orientation and drifting direction, and that some CP neurons, a subclass of CC neurons, were more broadly tuned than CT neurons. Compared with the electrophysiological study where neurons were classified by morphological reconstruction post hoc, our imaging-based approach used cell-type and projection specific labeling to identify CT and CP neurons, which enabled us to perform large-scale investigation of their activity in the awake mouse. We found both CP and CT neurons with drifting-grating-evoked responses with marked differences in their response properties: whereas 73% of visually-driven CT neurons were OS, only 39% of visually-driven CP neurons were; CT neurons were more direction selective than CP neurons and more likely to have well-defined receptive fields; both populations included sharply orientation-tuned cells, but CP also included more broadly tuned neurons. In contrast with a recent study that examined the functional properties of transgenically defined neuron populations (but not CP neurons) in the visual cortex and found the tuning properties of different types of excitatory neurons to be largely similar (de Vries et al. 2020), the marked differences between L6 CT and CP neurons in encoding visual features such as orientation, direction, and receptive field indicate that L6 CP neurons convey distinct information on the monocular visual field across corpus callosum into the contralateral hemisphere.

Performing activity measurements on CT and CP neurons in the awake mice, we discovered distinct activity patterns. Compared with CT neurons, the activity patterns for CP population were more dominated by spontaneous activity. Both during drifting grating stimuli and with the mice kept in the dark, CP neurons were much more likely than CT neurons to exhibit spontaneous activity (74% vs. 22% during grating stimuli, 93% vs. 59% in the dark) with larger mean $\Delta F/F$ values. The heightened spontaneous activity of CP population may be explained by its presynaptic input pattern. Whereas CT and CP populations both receive local V1 inputs, we found CP neurons to receive more long-range inputs from higher cortical areas of the ipsilateral hemisphere, which are likely feedback in nature and known to target deeper layers (Felleman and Van Essen 1991; Coogan and Burkhalter 1993; Rockland and Ojima 2003). They also received cross-callosal cortical inputs via the extensive CP neuron network revealed by the retrograde labeling experiments, with CP neurons from V1, secondary visual cortices, as well as primary auditory cortex projecting across corpus callosum into V1. Given the beliefs that spontaneous activity is primarily driven by corticocortical connections (Sanchez-Vives and McCormick 2000; Timofeev et al. 2000; MacLean et al. 2005) and projections from higher cortical regions initiate spontaneous patterns in deep layers of primary sensory cortex (Sakata and Harris 2009), these additional sources of cortical inputs for CP neurons may account for their heightened spontaneous firing.

These long-range cortical inputs, also observed recently in the somatosensory cortex (Zolnik et al. 2020), may provide complex (e.g., multisensory, higher cognitive) forces that drive and modulate the spontaneous firing of CP neurons (Tan 2015), in manners distinct from those of CT neurons. Whereas the correlation coefficients between the spontaneous activity and pupil diameter have similar distributions for CT neurons in the dark and during the presence of grating stimulation, the correlation of CP neurons' spontaneous activity with arousal become more pronounced with the presence of strong visual stimulation.

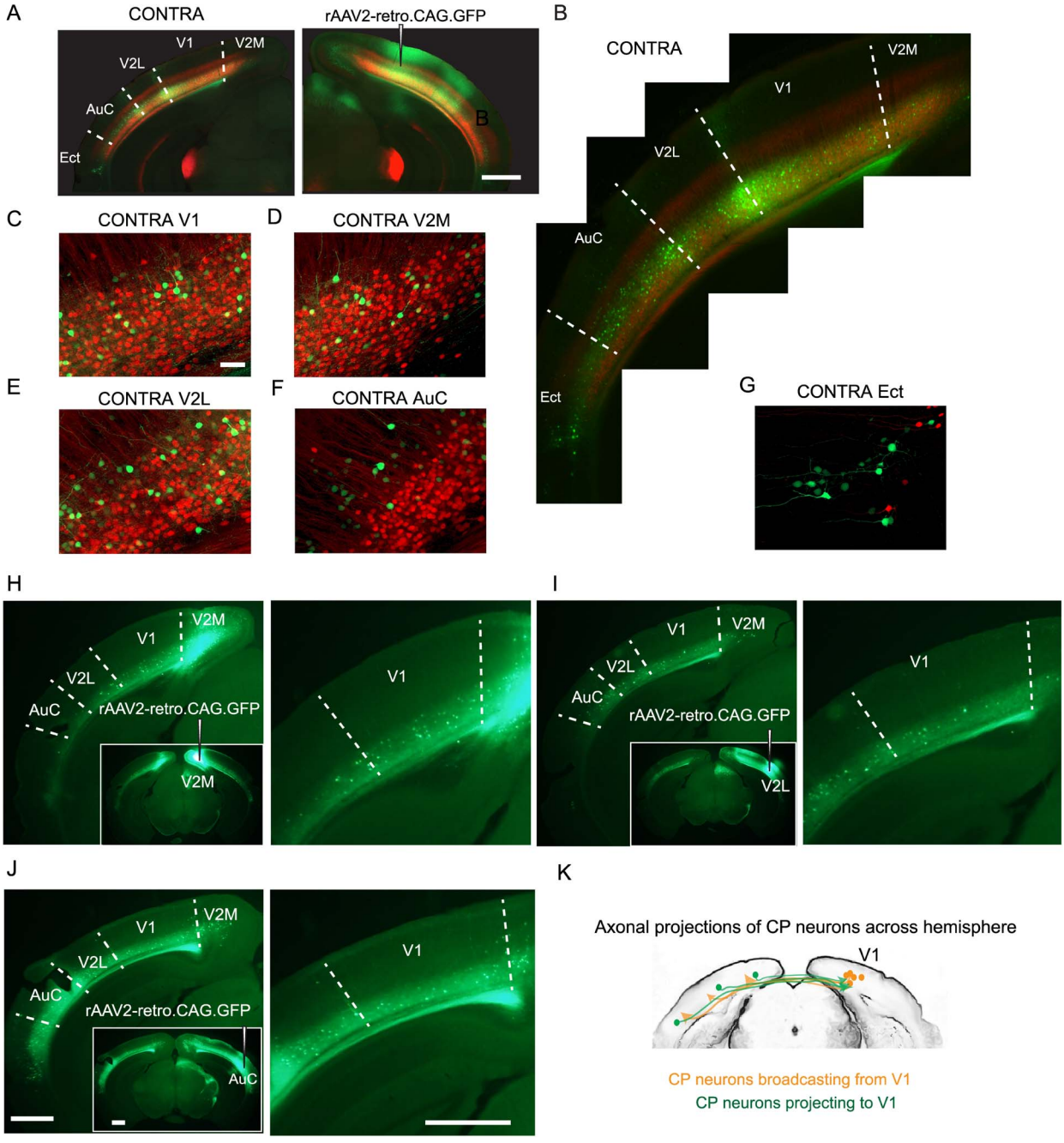

Figure 6. Extensive transcallosal projections to and from V1. (*A*) Unilateral injection of rAAV2-retro.CAG.GFP into right V1 of NTSR1-Cre × Ai14 mice, with CT neurons expressing tdTomato (red) and CP neurons in multiple cortical areas of the left hemisphere (contralateral side, CONTRA) labeled with GFP (green). (*B*) Contralateral (CONTRA) brain under high-zoom observation. (*C*-*G*) (left panels) Example coronal images of left V1 (*C*), V2M (*D*), V2L (*E*), AuC (*F*), and Ect (*G*). (*H*,*I*,*J*) Example coronal images (left panel) and zoomed-in views of V1 (right panel) of retrogradely labeled L6 CP neurons after injection of rAAV2-retro.CAG.GFP into V2M (*H*), V2L (*I*), or AuC (*J*). $n = 2$ mice for each group. (*K*) Schematic showing callosal projection patterns to and from V1. Scale bars: 1 mm in (*A*,*H*,*I*,*J*); 50 μm in (*C*–*G*).

For CT and CP neurons with spontaneous activity both in the dark and during grating stimuli, we found that their spontaneous activity was modulated by the presence of the grating stimuli. This is reminiscent of the finding that activity of corticocortical neurons in the awake rabbit motor cortex was modulated during changes in locomotion states (Beloozerova et al. 2003). It also parallels the observations made in alert macaque V1, where L6 were found to be the dominant spontaneously active layer both in the dark and in the light, with the change of illumination condition modulating their firing rates (Kayama et al. 1979; Snodderly and Gur 1995; Gur et al. 2005). Such changes of firing rate may encode the presence, timing, or luminance of a stimulus, as well as reflect the associated shifts of the animal's cortical and behavioral states.

The spontaneous activity patterns of the CP neurons are consistent with the cross-callosal reciprocal CP neuron network in the visual cortical area revealed by the retrograde tracing experiments. The involvement of higher visual cortices in this pathway may convey higher-level visual representations and provide contextual information and modulation to early processing of visual information in V1. The inclusion of AuC within this reciprocal network leads to the speculation that this network is also involved in cross-modal interactions across the hemispheres (Gau et al. 2020). Indeed, a recent work reported that visual stimuli can directly evoke activity of L6 neurons in auditory cortex (Morrill and Hasenstaub 2018), which may be partly attributed to the cross-callosal inputs from L6 CP neurons in visual cortices. Similarly, by conveying auditory information from the contralateral hemisphere, the transcallosal network described here can also contribute to the contextual modulation of V1 by auditory signals (Meijer et al. 2017; Petro et al. 2017).

Previous studies indicated that spontaneous events often originate from infragranular layers then spread upwards into superficial layers (Polack et al. 2007; Sakata and Harris 2009). In addition to leading to spontaneous activity in local V1 circuit and ipsilateral cortical regions, CP neurons also convey information to contralateral hemisphere through the corpus callosum, thus can influence cortical dynamics more globally. The exact functional roles of the spontaneous activity observed by us are unknown. Nevertheless, with their visually driven as well as spontaneous activity and given their extensive reciprocal network spanning multiple cortical areas in two hemispheres, L6 CP neurons are capable of broadcasting both visual and nonvisual information globally, thus may be involved in regulating and coordinating brain-wide activity events from sensory perception to memory replay (Petersen et al. 2003; Ji and Wilson 2007; Luczak et al. 2015).

Supplementary Material

Supplementary material can be found at *Cerebral Cortex* online.

Funding

The Howard Hughes Medical Institute (to Y.L., W.S., R.L., and N.J.); the National Natural Science Foundation of China (31700909 to M.C.); the National Institutes of Health (U19NS107613 to N.J. and J.L.F.).

Notes

We thank Jianhua Cang and Hillel Adesnik for helpful suggestions on the manuscript, Amy Hu for histology, and Kim Ritola for virus preparation. *Conflict of Interest*: The authors declare no competing interests. All data are available from the Lead Contact, Na Ji (jina@berkeley.edu), upon request.

References

Beloozerova IN, Sirota MG, Swadlow HA. 2003. Activity of different classes of neurons of the motor cortex during locomotion. *J Neurosci*. 23:1087–1097.

Bonin V, Histed MH, Yurgenson S, Reid RC. 2011. Local diversity and fine-scale organization of receptive fields in mouse visual cortex. *J Neurosci*. 31:18506–18521.

Bortone DS, Olsen SR, Scanziani M. 2014. Translaminar inhibitory cells recruited by layer 6 corticothalamic neurons suppress visual cortex. *Neuron*. 82:474–485.

Brown APY, Cossell L, Margrie TW. 2020. Excitatory and inhibitory L2/3 neurons in mouse primary visual cortex are balanced in their input connectivity. *bioRxiv* 2020.04.21.053504. doi: 10.1101/2020.04.21.053504.

Chen T-W, Wardill TJ, Sun Y, Pulver SR, Renninger SL, Baohan A, Schreiter ER, Kerr RA, Orger MB, Jayaraman V et al. 2013. Ultrasensitive fluorescent proteins for imaging neuronal activity. *Nature*. 499:295–300.

Coogan TA, Burkhalter A. 1993. Hierarchical organization of areas in rat visual cortex. *J Neurosci*. 13:3749–3772.

Cusick CG, Lund RD. 1981. The distribution of the callosal projection to the occipital visual cortex in rats and mice. *Brain Res*. 214:239–259.

Dana H, Mohar B, Sun Y, Narayan S, Gordus A, Hasseman JP, Tsegaye G, Holt GT, Hu A, Walpita D et al. 2016. Sensitive red protein calcium indicators for imaging neural activity. *Elife*. 5. doi: 10.7554/eLife.12727.

David SV, Vinje WE, Gallant JL. 2004. Natural stimulus statistics alter the receptive field structure of v1 neurons. *J Neurosci*. 24:6991–7006.

de Vries SEJ, Lecoq JA, Buice MA, Groblewski PA, Ocker GK, Oliver M, Feng D, Cain N, Ledochowitsch P, Millman D et al. 2020. A large-scale standardized physiological survey reveals functional organization of the mouse visual cortex. *Nat Neurosci*. 23:138–151.

Dehmel S, Lowel S. 2014. Cortico-cortical interactions influence binocularity of the primary visual cortex of adult mice. *PLoS One*. 9:e105745.

Elberger AJ. 1989. Selective labeling of visual corpus callosum connections with aspartate in cat and rat. *Vis Neurosci*. 2:81–85.

Fame RM, MacDonald JL, Macklis JD. 2011. Development, specification, and diversity of callosal projection neurons. *Trends Neurosci*. 34:41–50.

Felleman DJ, Van Essen DC. 1991. Distributed hierarchical processing in the primate cerebral cortex. *Cereb Cortex*. 1:1–47.

Franklin KBJ, Paxinos G. 2012. *The mouse brain in stereotaxic coordinates*. San Diego, CA: Academic Press.

Gau R, Bazin P-L, Trampel R, Turner R, Noppeney U. 2020. Resolving multisensory and attentional influences across cortical depth in sensory cortices. *eLife*. 9:e46856.

Gong S, Doughty M, Harbaugh CR, Cummins A, Hatten ME, Heintz N, Gerfen CR. 2007. Targeting Cre recombinase to specific neuron populations with bacterial artificial chromosome constructs. *J Neurosci*. 27:9817–9823.

Gur M, Kagan I, Snodderly DM. 2005. Orientation and direction selectivity of neurons in V1 of alert monkeys: functional relationships and laminar distributions. *Cereb Cortex*. 15:1207–1221.

Harris KD, Shepherd GM. 2015. The neocortical circuit: themes and variations. *Nat Neurosci*. 18:170–181.

Hlushchuk Y, Hari R. 2006. Transient suppression of ipsilateral primary somatosensory cortex during tactile finger stimulation. *J Neurosci*. 26:5819–5824.

Ji D, Wilson MA. 2007. Coordinated memory replay in the visual cortex and hippocampus during sleep. *Nat Neurosci*. 10:100–107.

Ji N, Milkie DE, Betzig E. 2010. Adaptive optics via pupil segmentation for high-resolution imaging in biological tissues. *Nat Methods*. 7:141–147.

Kayama Y, Riso RR, Bartlett JR, Doty RW. 1979. Luxotonic responses of units in macaque striate cortex. *J Neurophysiol*. 42:1495–1517.

Kobbert C, Apps R, Bechmann I, Lanciego JL, Mey J, Thanos S. 2000. Current concepts in neuroanatomical tracing. *Prog Neurobiol*. 62:327–351.

Lewis JW, Olavarria JF. 1995. Two rules for callosal connectivity in striate cortex of the rat. *J Comp Neurol*. 361:119–137.

Lien AD, Scanziani M. 2013. Tuned thalamic excitation is amplified by visual cortical circuits. *Nat Neurosci*. 16: 1315–1323.

Luczak A, McNaughton BL, Harris KD. 2015. Packet-based communication in the cortex. *Nat Rev Neurosci*. 16:745–755.

MacLean JN, Watson BO, Aaron GB, Yuste R. 2005. Internal dynamics determine the cortical response to thalamic stimulation. *Neuron*. 48:811–823.

Madisen L, Zwingman TA, Sunkin SM, Oh SW, Zariwala HA, Gu H, Ng LL, Palmiter RD, Hawrylycz MJ, Jones AR et al. 2010. A robust and high-throughput Cre reporting and characterization system for the whole mouse brain. *Nat Neurosci*. 13:133–140.

Marshel JH, Garrett ME, Nauhaus I, Callaway EM. 2011. Functional specialization of seven mouse visual cortical areas. *Neuron*. 72:1040–1054.

McGinley MJ, Vinck M, Reimer J, Batista-Brito R, Zagha E, Cadwell CR, Tolias AS, Cardin JA, McCormick DA. 2015. Waking state: rapid variations modulate neural and Behavioral responses. *Neuron*. 87:1143–1161.

Meijer GT, Montijn JS, Pennartz CMA, Lansink CS. 2017. Audiovisual modulation in mouse primary visual cortex depends on cross-modal stimulus configuration and congruency. *J Neurosci*. 37:8783–8796.

Morrill RJ, Hasenstaub AR. 2018. Visual information present in Infragranular layers of mouse auditory cortex. *J Neurosci*. 38:2854–2862.

Niell CM, Stryker MP. 2008. Highly selective receptive fields in mouse visual cortex. *J Neurosci*. 28:7520–7536.

Olavarria J, Van Sluyters RC. 1983. Widespread callosal connections in infragranular visual cortex of the rat. *Brain Res*. 279:233–237.

Olsen SR, Bortone DS, Adesnik H, Scanziani M. 2012. Gain control by layer six in cortical circuits of vision. *Nature*. 483: 47–52.

Payne BR, Siwek DF, Lomber SG. 1991. Complex transcallosal interactions in visual cortex. *Vis Neurosci*. 6:283–289.

Peron SP, Freeman J, Iyer V, Guo C, Svoboda K. 2015. A cellular resolution map of barrel cortex activity during tactile behavior. *Neuron*. 86:783–799.

Petersen CC, Hahn TT, Mehta M, Grinvald A, Sakmann B. 2003. Interaction of sensory responses with spontaneous depolarization in layer 2/3 barrel cortex. *Proc Natl Acad Sci U S A*. 100:13638–13643.

Petro LS, Paton AT, Muckli L. 2017. Contextual modulation of primary visual cortex by auditory signals. *Philos Trans R Soc Lond B Biol Sci*. 372. doi: 10.1098/rstb.2016.0104.

Pietrasanta M, Restani L, Caleo M. 2012. The corpus callosum and the visual cortex: plasticity is a game for two. *Neural Plast*. 2012:838672.

Polack PO, Guillemain I, Hu E, Deransart C, Depaulis A, Charpier S. 2007. Deep layer somatosensory cortical neurons initiate spike-and-wave discharges in a genetic model of absence seizures. *J Neurosci*. 27:6590–6599.

Ramos RL, Tam DM, Brumberg JC. 2008. Physiology and morphology of callosal projection neurons in mouse. *Neuroscience*. 153:654–663.

Reid RC, Shapley RM. 1992. Spatial structure of cone inputs to receptive fields in primate lateral geniculate nucleus. *Nature*. 356:716–718.

Rock C, Apicella AJ. 2015. Callosal projections drive neuronal-specific responses in the mouse auditory cortex. *J Neurosci*. 35:6703–6713.

Rockland KS, Ojima H. 2003. Multisensory convergence in calcarine visual areas in macaque monkey. *Int J Psychophysiol*. 50:19–26.

Sakata S, Harris KD. 2009. Laminar structure of spontaneous and sensory-evoked population activity in auditory cortex. *Neuron*. 64:404–418.

Sanchez-Vives MV, McCormick DA. 2000. Cellular and network mechanisms of rhythmic recurrent activity in neocortex. *Nat Neurosci*. 3:1027–1034.

Schindelin J, Arganda-Carreras I, Frise E, Kaynig V, Longair M, Pietzsch T, Preibisch S, Rueden C, Saalfeld S, Schmid B et al. 2012. Fiji: an open-source platform for biological-image analysis. *Nat Methods*. 9:676–682.

Shuler MG, Krupa DJ, Nicolelis MAL. 2001. Bilateral integration of whisker information in the primary somatosensory cortex of rats. *J Neurosci*. 21:5251–5261.

Snodderly DM, Gur M. 1995. Organization of striate cortex of alert, trained monkeys (Macaca fascicularis): ongoing activity, stimulus selectivity, and widths of receptive field activating regions. *J Neurophysiol*. 74:2100–2125.

Stryker MP, Antonini A. 2001. Factors shaping the corpus callosum. *J Comp Neurol*. 433:437–440.

Sun W, Tan Z, Mensh BD, Ji N. 2016. Thalamus provides layer 4 of primary visual cortex with orientation- and direction-tuned inputs. *Nat Neurosci*. 19:308–315.

Tan AY. 2015. Spatial diversity of spontaneous activity in the cortex. *Front Neural Circuits*. 9:48.

Tan Z, Sun W, Chen TW, Kim D, Ji N. 2015. Neuronal representation of ultraviolet visual stimuli in mouse primary visual cortex. *Sci Rep*. 5:12597.

Tervo DG, Hwang BY, Viswanathan S, Gaj T, Lavzin M, Ritola KD, Lindo S, Michael S, Kuleshova E, Ojala D et al. 2016. A designer AAV variant permits efficient retrograde access to projection neurons. *Neuron*. 92:372–382.

Timofeev I, Grenier F, Bazhenov M, Sejnowski TJ, Steriade M. 2000. Origin of slow cortical oscillations in deafferented cortical slabs. *Cereb Cortex*. 10:1185–1199.

Velez-Fort M, Rousseau CV, Niedworok CJ, Wickersham IR, Rancz EA, Brown AP, Strom M, Margrie TW. 2014. The stimulus selectivity and connectivity of layer six principal cells reveals cortical microcircuits underlying visual processing. *Neuron*. 83:1431–1443.

Vogelstein JT, Packer AM, Machado TA, Sippy T, Babadi B, Yuste R, Paninski L. 2010. Fast nonnegative deconvolution for spike train inference from population calcium imaging. *J Neurophysiol*. 104:3691–3704.

Wang Q, Burkhalter A. 2007. Area map of mouse visual cortex. *J Comp Neurol*. 502:339–357.

Wickersham IR, Finke S, Conzelmann KK, Callaway EM. 2007. Retrograde neuronal tracing with a deletion-mutant rabies virus. *Nat Methods*. 4:47–49.

Yorke CH Jr, Caviness VS Jr. 1975. Interhemispheric neocortical connections of the corpus callosum in the normal mouse: a

study based on anterograde and retrograde methods. *J Comp Neurol*. 164:233–245.

Zaidel E, Iacoboni M. 2003. *The parallel brain: the cognitive neuroscience of the corpus callosum*. Cambridge, MA: MIT Press.

Zhang ZW, Deschenes M. 1997. Intracortical axonal projections of lamina VI cells of the primary somatosensory cortex in the rat: a single-cell labeling study. *J Neurosci*. 17:6365–6379.

Zhao X, Liu M, Cang J. 2013. Sublinear binocular integration preserves orientation selectivity in mouse visual cortex. *Nat Commun*. 4:2088.

Zolnik TA, Ledderose J, Toumazou M, Trimbuch T, Oram T, Rosenmund C, Eickholt BJ, Sachdev RNS, Larkum ME. 2020. Layer 6b is driven by Intracortical long-range projection neurons. *Cell Rep*. 30:3492–3505 e3495.